# Distributed sensing for fluid disturbance compensation and motion control of intelligent robots

Michael Krieg<sup>1,2</sup>, Kevin Nelson<sup>0,2,3</sup> and Kamran Mohseni<sup>0,1,2,3</sup>\*

A control methodology for aerial or aquatic vehicles is presented that leverages intelligent distributed sensing inspired by the lateral line found in fish to directly measure the fluid forces acting on the vehicle. As a result, the complex robot control problem is effectively simplified to that of a rigid body in a vacuum. Furthermore, by sensing these forces, they can be compensated for immediately, rather than after they have displaced the vehicle. We have created a sensory shell around a prototype autonomous underwater vehicle, derived algorithms to remove static pressure and calculate total force from the discrete measurements using a fitting technique that filters sensor error, and validated the control methodology on a vehicle in the presence of multiple fluid disturbances. This sensing control scheme reduces position tracking errors by as much as 72% compared to a standard position error feedback controller.

he massive scale and highly dynamic nature of ocean environments make them ideal for inspection and study using fleets of autonomous sensor vehicles<sup>1</sup>. However, those same attributes, in addition to attenuation of radio and electromagnetic waves, make autonomous controller design challenging2. Many underwater vehicle controllers utilize some form of modelling to predict the significant forces imparted from the surrounding fluid. Often this modelling is done with respect to vehicle states<sup>3,4</sup>. Controllers utilize these models to predict forces and introduce additional control terms or adjust control gains in accordance and have been referred to as 'finite-dimensional plant model based control'. For a detailed summary of a six degrees of freedom (DOF) finite-dimensional plant-model-based controller see ref. 4. The model, which is based mainly on vehicle kinematics, is actually an approximation of the true fluid interaction forces, which depend on both the vehicle kinematics and the surrounding flow field (an infinite-dimensional continuous space). Furthermore, this approximation loses accuracy as the surrounding flow becomes more complex. Given the large ocean regions characterized by chaotic flow conditions, many recent studies have tried to take a more sophisticated approach to handling

In contrast to existing underwater robots, many fish and other organisms that live in chaotic littoral environments seem to manoeuver through turbulent waters with ease. Much of the success of these animals is due to both a multimodal propulsion scheme and distributed multimodal sensing, which allows them to adapt to a large range of environmental conditions<sup>5</sup>.

In fish, the mechanosensory stimulus comes from a system called the lateral line, which consists of an array of specialized hair cell receptors, or neuromasts (Fig. 1). These neuromasts are located both on the surface of the skin (superficial neuromasts, Fig. 1b) and in canals within the skin that are exposed to external flow through pores (canal neuromasts, Fig. 1c)<sup>6</sup>.

Researchers believe that the lateral line plays an integral role in many behaviours, such as schooling<sup>7,8</sup>, detection of obstacles and other organisms<sup>9</sup>, predation<sup>10,11</sup> and communication<sup>12</sup>. Observations

suggest that the physiology of the neuromasts diverged to provide sensitivity to complementary information about the surrounding fluid. Superficial neuromasts are believed to measure the relative flow velocity over the skin of the organism<sup>13,14</sup>, whereas canal neuromasts measure the acceleration of the fluid<sup>15</sup>.

Seeing the benefit that the lateral line provides to aquatic organisms has inspired many researchers to attempt to replicate the sensing capabilities of this system for use in robotic applications. Some researchers have fabricated custom sensors to perform various tasks such as measuring flow rates 16,17 and detecting dipoles 18,19. In ref. 20, a linear array of pressure sensors was used to determine the position, shape and size of various objects in a flow. Venturelli and colleagues<sup>21</sup> attempted to use absolute pressure sensors to detect the turbulent wake of a cylinder; these sensors suffered from low resolution, requiring amplification and high-precision analog-todigital converters to achieve moderate sensor resolution. Ren and Mohseni derived algorithms to identify bluff body wake structures<sup>22</sup> and detect nearby walls<sup>23</sup>, which were verified using simulated flows around fish bodies. The wall detection algorithm was then experimentally validated using an artificial lateral line system consisting of distributed differential pressure sensors<sup>24</sup>. In ref. <sup>25</sup>, a similar artificial lateral line system was used to calculate the hydrodynamic forces acting on the surface of a rigid body in constrained motion. In ref. 26, researchers demonstrated that an artificial lateral line system can be used to monitor the speed and acceleration of a marine craft; however, the estimation error tended to scale with velocity, suggesting it is not suitable for fast-moving vehicles. In another work, a lateral line system utilizing pressure sensors was used to detect the angle of attack of a marine craft for use in active yaw control; this system achieved reasonable results after advanced filtering techniques were applied27. Recently, a lateral-line-inspired sensory system installed on a moving hydrofoil in a water tunnel was used to perform Kármán gaiting<sup>28</sup>.

Parallels can be drawn between fish rheotaxis and feedback control of autonomous systems. Rheotaxis is a behaviour involving the lateral line, as well as optical and tactile sensing, whereby a fish

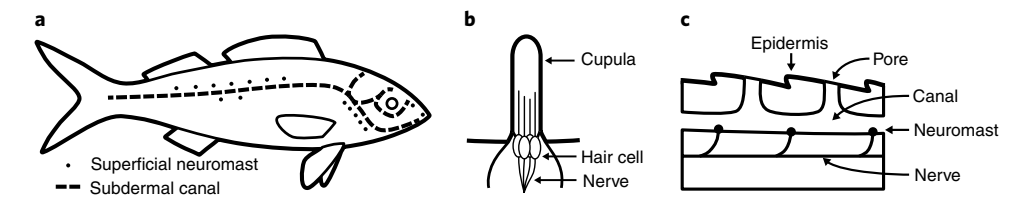


**Fig. 1** | The lateral line found in fish is composed of two types of specialized sensory organ called neuromasts. Superficial neuromasts are located on the body surface, whereas canal neuromasts are located inside subdermal canals. **a**, Typical layout of the lateral line system and locations of neuromasts. **b**, Diagram of a superficial neuromast. **c**, Diagram of neuromasts in a subdermal canal.

realigns itself into the direction of oncoming flow<sup>29</sup>. Using sight and touch, fish identify their position within their surroundings. Fluid currents are both sensed by the lateral line and inferred by displacement of the body within the surroundings, allowing the fish to reorient. As was shown in ref. <sup>30</sup>, the velocity threshold for a current to elicit a rheotactic response is four to ten times larger if the lateral line signals are blocked. The improved response observed with a functional lateral line occurs because optical and tactile sensing can only infer the existence of a current due to the resulting body displacement, whereas the lateral line senses those currents directly. Furthermore, the fish is able to react to the flow before it results in a significant body displacement, thus improving performance.

Typically, vehicle controllers utilize sensing that determines vehicle states relative to some inertial reference (for example, optical sensors, inertial measurement sensors, GPS receivers and so on). Much like fish performing rheotaxis, vehicles infer the existence of fluid disturbances from a measured displacement that is inconsistent with the commanded control. Because disturbances are measured indirectly through vehicle displacement, disturbance rejection can be improved by measuring forces directly, similar to rheotaxis in fish. However, because the fluid interacts across the entire surface of the vehicle, a distributed sensory system is required to accurately measure these fluid interactions.

We first proposed the idea of using a bioinspired distributed pressure sensory system as a feedforward control element in ref. <sup>25</sup>. That paper compared simulation results of a force feedforward controller with a robust integral of the sign of the error (RISE)-based feedback controller, and showed a decrease in position tracking error. Although that study examined the control technique through simulation, the current study study performs hydrodynamic force compensation on a freely swimming autonomous underwater vehicle (AUV) with experimentally generated fluid disturbances. The ability of the sensory system to measure hydrodynamic forces was validated on a prototype with pressure sensors embedded into the hull<sup>24</sup>. We presented a modular sensor shell that fits on the surface of an AUV and showed that it is capable of sensing hydrodynamic forces on a body constrained to one DOF<sup>31</sup>.

In this study, we experimentally show the benefit of directly compensating for measured forces in low-level-motion controllers. Because corrective action is taken prior to vehicle displacement, position tracking is significantly improved and the technique simplifies the vehicle dynamics, effectively reducing the control problem to that of a rigid body in a vacuum. The algorithm for calculating the hydrodynamic forces from the differential pressure distribution is presented along with the proposed force compensation control algorithm. We show that the combination of this feedforward term and proportional-derivative (PD) state feedback is sufficient to provide exponential stability to an underwater vehicle in the presence of arbitrary disturbances. We then experimentally verify the control strategy on a freely moving vehicle in a large testing tank in the presence of disturbances and compare the position tracking results to traditional feedback controllers. Although other researchers have

presented works on artificial lateral line sensory systems, this paper presents a lateral-line-inspired, hydrodynamic force measurement system used within a low-level-motion controller, which is a fundamentally different application. Other proposed applications use the enhanced detection capabilities to help inform mission level and path planning decisions<sup>24,32,33</sup>.

This Article begins with a summary of underwater vehicle control techniques and how the proposed methodology relates to those techniques. Next, the testing results are analysed to validate the proposed technique. Finally, the exact methods used to perform testing are provided.

## Novel methodology for intelligent vehicle locomotion

To illustrate the novelty of our methodology, this section discusses how the proposed control methodology compares with traditional model-based control strategies. A historical context of underwater vehicle control development is presented, identifying ways that fluid forces are addressed. Next we show how these techniques degrade with increasing flow complexity, and describe the need for a novel methodology leveraging a distributed sensory system to measure the fluid forces and moments in a complex flow.

**Control summary and motivation.** The most general formulation of underwater vehicle dynamics is given by the governing equations for a rigid body, with an additional term for hydrodynamic forces:

$$M_{\rm RB}\dot{\nu} + C_{\rm RB}(\nu)\nu + \mathbf{F}_{\rm D} = \tau \tag{1a}$$

$$\dot{\boldsymbol{\eta}} = J(\boldsymbol{\eta})\boldsymbol{\nu} \tag{1b}$$

where the vector  $\eta \in \mathbb{R}^n$  contains the position and orientation of the vehicle in the inertial frame and  $\nu \in \mathbb{R}^n$  contains the linear and angular velocity of the vehicle expressed in the body-fixed frame with n representing the number of states.  $M_{\text{RB}} \in \mathbb{R}^{n \times n}$  is a matrix containing the inertial terms of the rigid body,  $C_{\text{RB}} : \mathbb{R}^n \to \mathbb{R}^{n \times n}$  is a matrix containing the Coriolis/centrifugal terms of the rigid body, which is a function of the body rotational and linear velocities,  $\mathbf{F}_D \in \mathbb{R}^n$  represents the vector of fluid forces acting on the vehicle, the vector  $\tau \in \mathbb{R}^n$  denotes the control forces and moments, and  $J : \mathbb{R}^n \to \mathbb{R}^{n \times n}$  represents the velocity transformation from the body-fixed frame to the inertial frame.

Historically, forces between solid bodies and surrounding fluids have been investigated in wind or water tunnels where the incoming flow is maintained as uniform as possible. Obviously, the flow becomes non-uniform as it moves over the body, but the resulting flow will be consistent for a given body orientation and incoming velocity. Thus, the flow and resulting forces are characterized by a single parameter, the tunnel flow velocity (and its derivative). Hence, wind/water tunnel characterization of fluid forces is inherently vehicle attitude dependent. Subsequently, viscous forces (that is, drag) are characterized by flow velocity, and are observed to be

proportional to the velocity squared. Other forces that only exist in oscillating/unsteady flows, and scale with flow acceleration, are termed 'added mass' because they act like additional inertia resisting body acceleration. This leads to the dynamics of underwater vehicles generally being modelled by the following set of differential equations in terms of the vehicle states<sup>34</sup>:

$$M_{\mathrm{RB}}\dot{\nu} + C_{\mathrm{RB}}(\nu)\nu + M_{\mathrm{A}}\dot{\nu} + C_{\mathrm{A}}(\nu)\nu + D(\nu)\nu + G(\eta) + \tau_{\mathrm{dist}} = \tau \qquad (2\mathrm{a})$$

$$\dot{\boldsymbol{\eta}} = J(\boldsymbol{\eta})\boldsymbol{\nu} \tag{2b}$$

where  $M_A \in \mathbb{R}^{n \times n}$  represents the added mass matrix of the fluid,  $C_A : \mathbb{R}^n \to \mathbb{R}^{n \times n}$  is the Coriolis/centrifugal terms of the added mass,  $D : \mathbb{R}^n \to \mathbb{R}^{n \times n}$  represents the drag terms,  $G : \mathbb{R}^n \to \mathbb{R}^n$  represents the restoring forces, and  $\tau_{\text{dist}} \in \mathbb{R}^n$  represents the unmodelled fluid disturbance forces and moments. Due to communication limitations, underwater vehicle control systems have relied heavily on inertial measurement sensors  $^{35}$ , and more recently sonar and optical simultaneous localization and mapping (SLAM) $^{36,37}$ , to determine vehicle states. Fluid force estimators used to improve controller performance have naturally assumed the form of equations (2a) and (2b). As such, significant effort has gone into modelling hydrodynamic force coefficients  $^{34}$ .

The kinematic representation of hydrodynamic forces (2a) and (2b) is straightforward, but there are two main issues with this representation. First, this model is just a convenient construct and not necessarily representative of the physics involved. In reality, there are no 'drag' or 'added mass' forces. The surrounding fluid transfers momentum and energy to the vehicle through a distribution of pressure and shear stresses on the vehicle surface. The total hydrodynamic forces are then the spacial integral of the pressure and shear distributions. Furthermore, the distribution of pressure and shear stresses over the body is dependent on the entire surrounding flow field, which can only be represented by a single relative velocity for a uniform flow over the body. In other words, the hydrodynamic forces are not, in general, a function of the six rigid body states (and their derivatives), but rather a function of an infinite number of fluid environmental states. In a more general sense, determining any integral quantity, like fluid dynamic force, from a single sensor measurement will require substantial assumptions, such as a prescribed distribution shape, which inherently limits accuracy.

The other issue with the body-kinematics representation of the hydrodynamic forces is that, even for restrictive cases of uniform flow over the body, the drag terms are nonlinear functions of the vehicle velocity. This makes it more difficult to model the robot behaviour and impossible to generate an accurate linear timeinvariant (LTI) model of the system to perform frequency response analysis, without making several simplifications and linearizing about trim conditions38. If, instead, hydrodynamic forces are compensated using a feedforward control term, the dynamics become a linear function of vehicle states, as in the rigid body dynamics (1a) and (1b) as opposed to the kinematic based force model (2a) and (2b). The force compensation technique also greatly simplifies the job of the designer selecting the controller gains, because the inertial forces, unlike hydrodynamic forces, only depend on the physical properties of the vehicle (like mass and the moments of inertia). The additional controller parameters thus only need to be tuned for the rigid body system, while controllers and estimators without intelligent sensing need to adapt the control parameters to provide the desired behaviour at different trim conditions.

Several control techniques have been employed to account for hydrodynamic forces, including disturbance velocity estimators<sup>39</sup>, sliding mode<sup>40,41</sup> and adaptive<sup>42</sup> controllers, Kalman filter based velocity/disturbance estimators<sup>43</sup> and neural network or machine

learning based estimators<sup>44,45</sup>. These techniques have varying degrees of success, but they ignore the fact that they are trying to determine an integral quantity from a single value measurement (that is, the velocity of the vehicle). If there is no unique solution for hydrodynamic forces with respect to a given set of vehicle inertial sensor measurements, they cannot be calculated, no matter how well the adaptive models or learning algorithms are designed. This issue is avoided by the technique presented here where the fluid forces are measured directly and passed to the controller.

Next we discuss the control laws used in testing. Additional analysis of the control methods and their stability is presented in the Supplementary Discussion.

**PD** controller with hydrodynamic force feedforward. Much in the same way a fish feels the flow around its body and reacts instinctively, allowing it to overcome fluid disturbances effortlessly, an autonomous robot patterned with pressure and shear sensors can measure the distribution of those quantities over its surface and immediately respond to fluid disturbance forces. Here we present the control laws for this methodology, shown as a block diagram in Supplementary Fig. 1.

Provided the hydrodynamic forces,  $F_D$ , can be accurately measured and do not exceed the control authority of the system, a controller can be designed as

$$\tau = \mathbf{F}_{\mathrm{D}} + \tau_{\mathrm{FB}} \tag{3}$$

where  $\tau_{FB} \in \mathbb{R}^n$  is a stabilizing error feedback controller with the assumption that the sum of the feedforward and feedback signals does not exceed the thruster capacity. Here we use a simple PD feedback controller, which can be designed as

$$\boldsymbol{\tau}_{\mathrm{FB}} = J^{-1}(\boldsymbol{\eta})(K_{\mathrm{p}}\mathbf{e}_{1} + K_{\mathrm{d}}\mathbf{e}_{2}) \tag{4}$$

where  $K_p$ ,  $K_d \in \mathbb{R}^{n \times n}$  are diagonal matrices of positive, constant gains,  $\mathbf{e}_1 = \mathbf{\eta}_d - \mathbf{\eta}$  is the position error of the system, and  $\mathbf{e}_2$  is the derivative of  $\mathbf{e}_1$ , that is, the velocity error.

After combining equations (1a), (1b) and (3), the complexity of the control problem is reduced to the control of a rigid body in a vacuum under a given external forcing:

$$M_{\rm RB}\dot{\nu} + C_{\rm RB}(\nu)\nu = \tau_{\rm FB} \tag{5}$$

which is much easier to model and control than the general formulation.

**Theorem 1:** If the hydrodynamic forces are measurable and bounded, then the controller given by (3) with feedback controller (4) exponentially stabilizes the system (1a) and (1b) in the sense that  $\|\mathbf{e}_1\| \to 0$  as  $t \to \infty$ , assuming sufficient choices of gains  $K_p$  and  $K_d$ .

*Proof.* The proof of Theorem 1 is provided in the Supplementary Information.

We have shown that the new hydrodynamic force feedforward controller is globally exponentially stable, but it requires that the hydrodynamic forces are being measured directly. An accurate real-time measurement of those hydrodynamic forces will require a system of sensors distributed over the entire surface of the vehicle.

## Results

To experimentally validate the proposed control scheme we created a modular lateral line sensor shell that fits over the surface of a pre-existing AUV (called CephaloBot<sup>46</sup>) created by our group (Fig. 2). Sensor modules are flush with the shell surface to minimize their impact on drag (Fig. 3). The vehicle is placed in a large testing tank equipped with a wave disturbance generator and attempts to



Fig. 2 | Photographs of the modular lateral line sensory system and the AUV used in the experimental data collection. a, Photograph of our AUV, CephaloBot. b, Lateral line sensing shell consisting of a 3D printed scaffolding, distributed sensor modules and a centralized processor module. c, Photograph of the lateral line system fully assembled on CephaloBot.

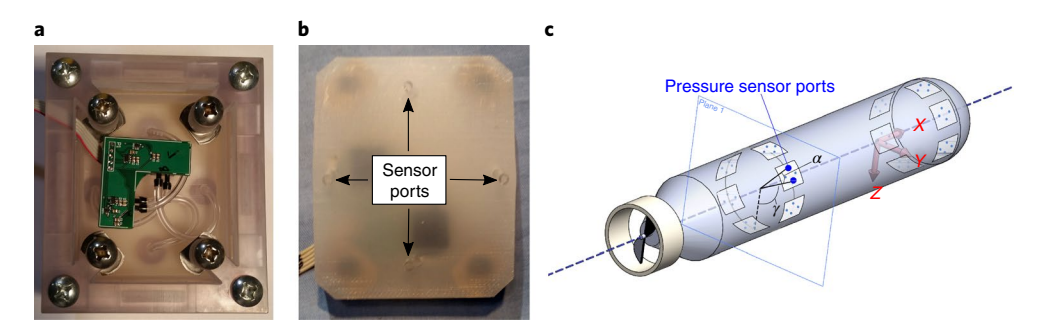


**Fig. 3** | Images showing individual sensor fabrication and their layout on the vehicle surface. **a**, Each sensor module contains a pair of differential pressure sensors mounted on an electronics board. **b**, The board is embedded in elastomer with hardware that allows it to connect to the 3D printed scaffolding. **c**, Illustration of the prototype AUV used in this experiment including the definition of the body fixed reference frame, and the internal angles related to the pressure sensor distribution. These angles are defined such that  $\alpha$  is the port separation of the differential pressure sensors and  $\gamma$  is the angle from the z axis to the midpoint of the sensor module.

maintain position while being impacted by unsteady disturbances. A desktop computer located on the platform above the tank was used to run a motion capture system that passed data to various station-keeping motion controllers. A detailed description of all the equipment used in this testing and the data processing procedures are provided in the Methods. Figure 4 shows the AUV in the testing set-up. We collected several sets of vehicle position data while attempting to hold position in the presence of disturbances for each of the controller types.

Controller performance comparison. The wave generator created multiple types of disturbances by varying the frequency and amplitude of oscillation. The means and standard deviations of the amplitude and frequency are reported in Table 1. The first disturbance condition is a large-amplitude low-frequency wave, while the second disturbance condition is higher-frequency waves with lower amplitude. Although both disturbance cases create unsteady forces, the large vehicle inertia acts to filter out high-frequency oscillations in position. Figure 5a shows the AUV trajectory while passively drifting with the flow under both disturbance conditions. It can be seen that the lower-frequency disturbance results in larger fluctuations in vehicle position, while the higher-frequency disturbance maintains a more consistent drift velocity.

The controller cases examined in the study are as follows: baseline of the vehicle without control (Passive), a standard proportional derivative controller (PD), a standard proportional integral derivative controller (PID) and a proportional derivative controller combined with the lateral line feedforward term (LLFF). For all trials, the error feedback gains were held constant. The gains were chosen based on the tuning performed in ref. <sup>47</sup> and are  $K_p = [5, 4, 3]^T$ ,  $K_d = [1, 1.25, 0.5]^T$  and  $K_i = [0.25, 0.25, 0.25]^T$  in the surge, sway and yaw directions, respectively.

The current lateral line shell is designed for estimating hydrodynamic forces in the body *y* axis (sway). Similarly, the disturbance generator is designed to create waves that impact the vehicle uniformly over its length, despite large variations in flow field with respect to the radial and azimuthal directions. Thus, we will focus on the position tracking error in the sway direction. The mean sway error, root-mean square (r.m.s.) sway error and standard deviations of these errors for each of the controllers are reported in Table 1. Figure 5c depicts the mean sway error as a function of time for all four control cases and disturbance condition 1 and Fig. 5d shows mean sway error for disturbance condition 2. Note that the wave generator was only driven for five cycles because continued flapping moved the AUV out of range of the motion capture system for some cases, and we wanted to generate consistent disturbances for all cases.

In terms of mean sway error, averaged over the duration of the trials, the lateral line feedforward controller outperforms the PID and PD controllers by about 72% and 82%, respectively, for lowerfrequency disturbances, and results in 59% and 73% less sway error than PID and PD controllers for higher-frequency disturbances. As can be seen from Fig. 5, the drastic improvement is largely due to the robot's ability to sense the disturbance force and provide a compensation force before the vehicle moves away from the desired position. By contrast, the PD controller allows the AUV to be displaced by more than 600 mm before the proportional feedback term overpowers the disturbances and begins to move the AUV back to the desired position. Furthermore, both feedback control cases are displaced at nearly the same rate as the passive case for the first several seconds. The PID control does better, but the integral of the position error must build up over time before the control command can overcome the disturbances.

The force compensation technique shows a more relative improvement for the lower-frequency disturbances for two reasons.

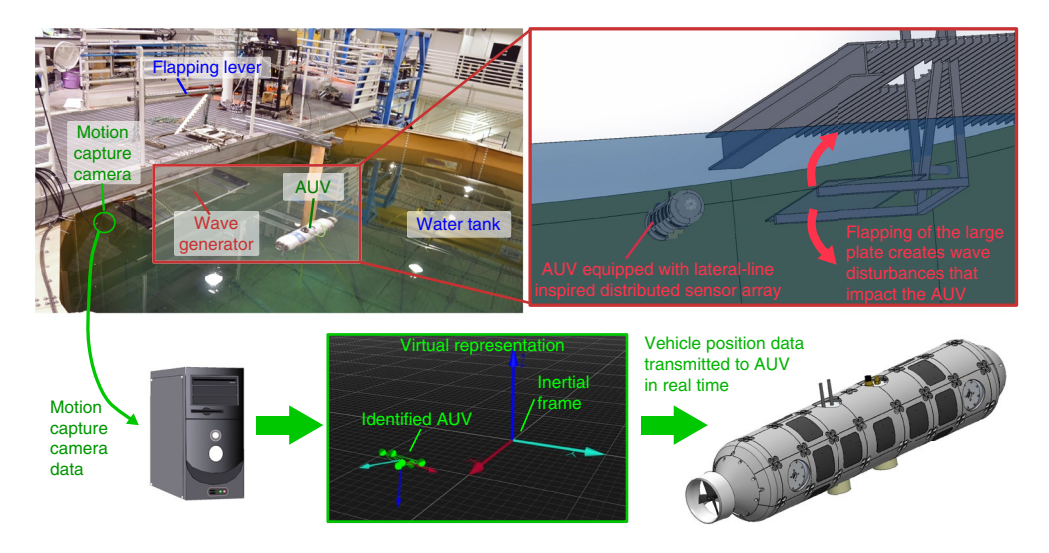


Fig. 4 | The CephaloBot AUV<sup>46</sup> with the distributed hydrodynamic sensing system, shown in the vehicle testing tank next to the wave generator used to provide unsteady sway disturbances. Vehicle position and orientation are measured throughout test runs by an underwater motion capture system. Extensive details of this experimental set-up are provided in ref. <sup>47</sup>.

Since the high-frequency disturbance results in vehicle displacement similar to that in a uniform flow (Fig. 5), the PID controller is more effective. In addition, the larger-amplitude force oscillation of the lower-frequency disturbances improves the signal-to-noise ratio of the pressure measurement.

Although PD/PID controllers were used as a base comparison reference during experimentation due to their ubiquitous use in robotics, there are more sophisticated control algorithms that are common in underwater robotics, such as sliding mode and adaptive sliding controllers. Because the focus of this work is introducing novel force compensation techniques, the development and discussion of more complicated controllers for the prototype AUV are beyond the current scope. However, we created a simulation of a one DOF cylindrical AUV with nonlinear drag modelling, which estimates the relative performance of more sophisticated controllers. Similar to empirical testing, the AUV was subjected to periodic disturbance forces and attempts to maintain position. The details of the simulation and results are provided in full in the Supplementary Information. As a summary, the relative improvement of the force compensation control over PID is consistent with the experimental data, and the performances of the sliding mode and adaptive controllers are very sensitive to the nature of the disturbance. Although these controllers can provide tracking performance consistent with the force compensation technique for uniform disturbance flows, the lateral line feedforward control shows 72% and 85% improvement over the sliding mode and adaptive controllers for more complex disturbances. Furthermore, we designed an adaptive controller that utilizes the lateral line force measurements, which produces a control law very similar to the lateral line feedforward control. This control showed an additional 33% improvement over the force compensation control used in experimental testing.

### Discussion

We have presented a novel sensing and control methodology for mobile robots in fluid environments, in which hydrodynamic forces are directly measured using a distributed sensory system on the robot surface, and compensated for instantly. If done correctly, this hydrodynamic force feedforward system decouples the rigid body dynamics from the complicated fluid structure interactions, reducing the control problem to that of a rigid body in a vacuum. To validate this theory, we created an external shell for the AUV consisting of arrays of pressure sensors, allowing the AUV to feel

**Table 1** | Summary of control and disturbance conditions for test sets, and the resulting position tracking stability

Control	n	а <sub>н</sub> (mm)	f (Hz)	Mean sway error (mm)	R.m.s. sway error (mm)
Passive 1	4	178 ± 17	$0.23 \pm 0.04$	$712 \pm 143$	816 ± 160
PD1	7	$180 \pm 19$	$0.23 \pm 0.01$	$431 \pm 194$	$493 \pm 216$
PID 1	9	173 ± 19	$0.24 \pm 0.02$	$278 \pm 110$	$318 \pm 126$
LLFF 1	5	181±5	$0.26 \pm 0.01$	$78 \pm 54$	$85 \pm 62$
Passive 2	4	$135 \pm 15$	$0.33 \pm 0.03$	$950 \pm 197$	$1073 \pm 209$
PD 2	6	$135 \pm 23$	$0.31 \pm 0.04$	$432 \pm 203$	$466 \pm 230$
PID 2	5	$134 \pm 18$	$0.33 \pm 0.02$	$291 \pm 78$	$316 \pm 80$
LLFF 2	5	127 ± 14	$0.32 \pm 0.02$	119 ± 81	121 ± 86

Tests are organized according to the control algorithm employed; n is the number of tests for each control case,  $a_n$  is the amplitude of the wave generator oscillation (at the root) and f is the frequency of the flapping oscillation. The error for each control case is averaged over all experimental trials.

the surrounding flow, and performed hydrodynamic disturbance rejection experiments in our large testing tank. The lateral line controller reduced the mean sway error by 72% compared to a PID controller for lower-frequency disturbance waves, and reduced sway error by 59% compared to PID controllers for higher-frequency disturbances. This significant performance improvement validates our theoretical stability analysis and shows a clear advantage of using a hydrodynamic force sensory system in a vehicle controller. This advantage is due to a much more natural stimulus-response approach. Rather than indirectly inferring the existence of a fluid disturbance due to an observed displacement of the vehicle, the AUV feels the disturbance force on the 'skin' of the vehicle and performs corrective action simultaneously. Because vehicle displacement is no longer required to identify a disturbance, the vehicle can maintain its position much more accurately.

In the section 'Comparison of static and dynamic forces' of the Supplementary Information, we discuss the relative magnitudes of the static pressure force component, illustrating how important an accurate technique for removing the static pressure component is to the overall force compensation technique. We separated the sway forces experienced by the AUV, throughout the entire testing, into static and dynamic components to show the relative magnitudes of

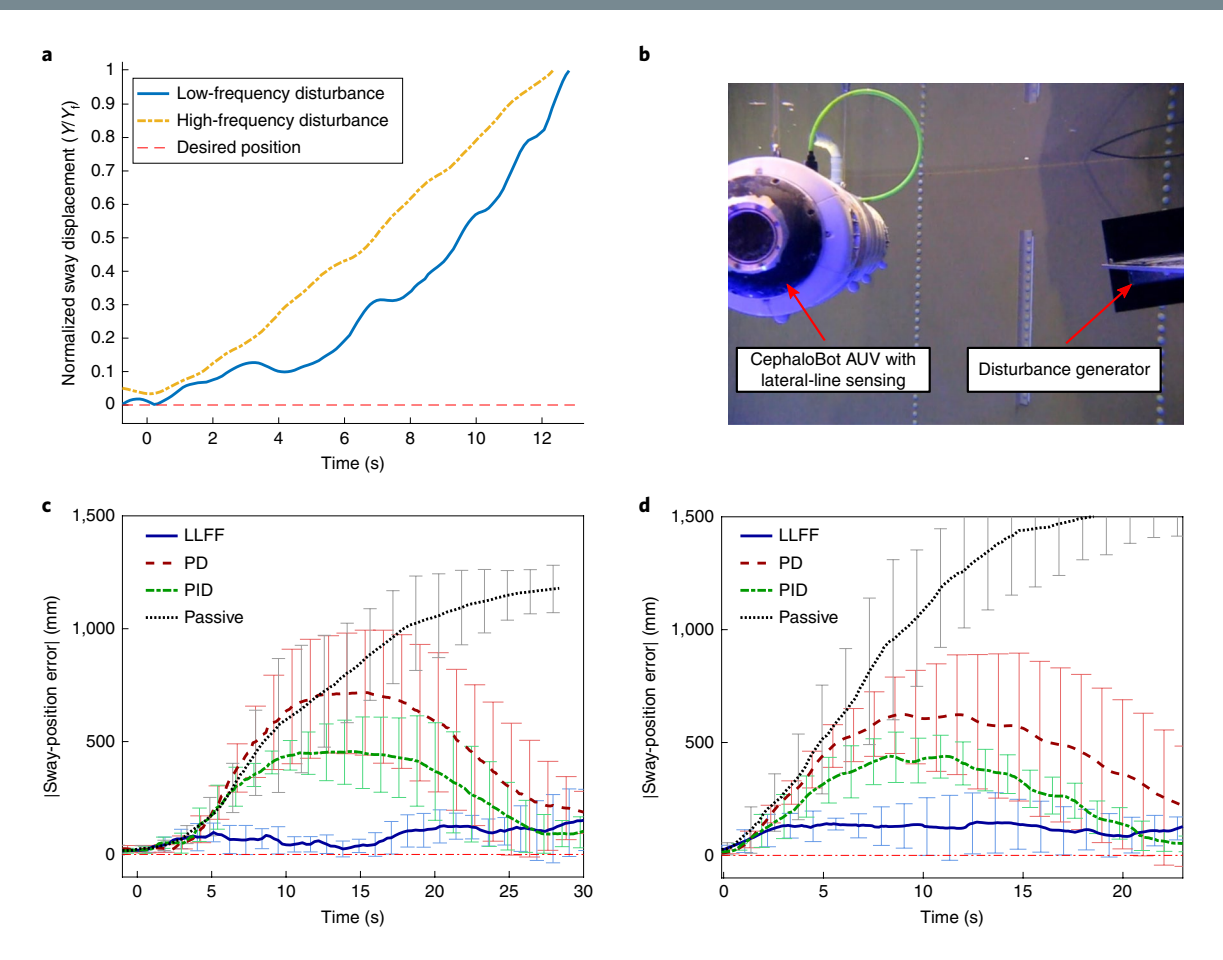


**Fig. 5 | Vehicle trajectory and position tracking results. a**, Passive vehicle displacement due to the different disturbance conditions. Two representative example vehicle trajectories for individual trials are shown rather than the average trajectory to show the effect on passive vehicle response of the different types of disturbance. For both cases, the vehicle is passively drifting with the flow (no control forces are imposed). The displacement is normalized by the final displaced position for easier comparison of the effect disturbance frequency has on vehicle motion. The lower-frequency disturbance results in larger oscillations in position, and the higher-frequency disturbance results in more consistent drift velocity due to the effect of vehicle inertia. **b**, The AUV is shown next to the wave generator during testing to show the proximity of the vehicle to the source of the disturbance flow. **c,d**, Mean error comparison between different controllers in the presence of hydrodynamic disturbances. Data sets are normalized so that the initial time corresponds to when the first hydrodynamic disturbance begins interacting with the vehicle. The mean sway error is reported for each controller, with error bars indicating the standard deviation of the error. Sway errors for disturbance condition 1 are shown in **c** and for disturbance condition 2 in **d**.

each. The majority of measured dynamic forces occur below 18 N, whereas the component of buoyancy force in the sway direction regularly exceeds 40 N, even reaching as high as  $100\,\mathrm{N}$ . This analysis demonstrates how an accurate method of removing the static pressure from the lateral line measurements is necessary for successful hydrodynamic force compensation, as even small changes in attitude can produce large buoyancy forces in the sway direction that are already compensated for by the weight force.

Even though this novel methodology was described and validated in terms of an underwater vehicle, it has much wider reaching implications. For example, if similar intelligent distributed sensory systems were applied to the wings and control surfaces of aircraft, they could measure the exact forces on these control surfaces directly rather than relying on stability derivatives, which, like underwater hydrodynamic forces, are typically linearized about some trim condition and not well modelled in complex flows.

# Methods

The experimental testing of this investigation consisted of a freely swimming AUV submerged in a large water tank that attempted to hold a desired position while being impacted by fluid disturbances generated in the tank. The in-house developed AUV platform was outfitted with a custom distributed lateral line sensor shell to measure the hydrodynamic forces. In this section we describe the

prototype AUV, the various apparatus used to localize the vehicle and generate disturbances, and the lateral-line-inspired distributed sensor shell.

**Testing facilities.** The experimental validation of the direct force compensation methodology was performed in a 225,000 l water tank located in our laboratory. The tank is shown in Fig. 4. A platform overhangs the tank, which allows access to the water. The tank is 7.6 m (25 ft) in diameter and 4.6 m (15 ft) deep. A wave generator is mounted to the platform and can be manually rocked back and forth to produce disturbance waves during testing.

A Qualisys underwater motion capture system, consisting of four waterproof OQUS 5 cameras, was used to localize the vehicle during testing. Based on system calibration, the three-dimensional (3D) positions of the vehicle were measured with a residual error of  $\sim\!2$  mm and corresponding angular error. These state measurements were sent to the motion controller and used for calculating feedback to the vehicle. The benefit of the motion capture system in this study is that it not only tracks the vehicle trajectory used for performance analysis, but also provides the controller with vehicle states in real time. Locating the vehicle position with respect to an inertial reference is a significant challenge in underwater robot control, but is not a focus of the current study. Use of the motion capture system allows us to isolate errors in position due to a specific control strategy from those errors that arise from uncertainty in vehicle states.

**Wave generator.** The hydrodynamic disturbances were created by a wave generator consisting of an oscillating flat plate, which was first developed and reported in ref. <sup>47</sup>. The wave generator is made of an acrylic plate mounted to 80/20 and unistrut framing material with a pair of hinges that connect to the platform above the tank. Given the geometry of the wave generator, the pitching and

heaving motions are coupled. As the plate oscillates, it produces one or more horseshoe vortices. Because the wave generator was designed to have a longer span than the vehicle length, we assume that the centre of the flow (where the vehicle is operating) can be approximated as a 2D reverse Kármán vortex street. Although this flow varies with both position and time, the translational velocity of the vortices is a function of the amplitude of oscillation,  $a_{\rm H}$ , and the frequency of oscillation, f. Based on the structure of the flow, we are able to relate the translational velocities of the vortices to the disturbance velocity (or relative velocity of the flow) experienced by the vehicle<sup>17</sup>. We found that the disturbance velocity is approximately proportional to the product of the amplitude and frequency of the oscillation:

$$V_{\text{dist}} = C_{\text{w}} a_{\text{H}} f$$

where  $C_w = 27.16$  is an empirically fitted coefficient <sup>47</sup>. A disturbance force can be estimated from the disturbance velocity after making simplifying assumptions. Additional details on the disturbance generator are provided in the Supplementary Information.

**CephaloBot AUV prototype.** The station keeping experiment was performed on our in-house-developed AUV, CephaloBot. CephaloBot is a torpedo-shaped AUV designed and manufactured by our group and is shown in Fig. 2. CephaloBot is 1.12 m (44 in) in length and 0.152 m (6 in) in diameter. Extensive details describing CephaloBot's design and systems are provided in ref. <sup>46</sup>.

CephaloBot can generate control forces in surge, sway and yaw; it is equipped with a rear propeller to provide surge control forces and four thrusters embedded within each side of the hull both fore and aft, providing lateral forces. The thrusters, which draw inspiration from the locomotion of jellyfish and cephalopods, successively ingest and expel jets of water from an internal cavity through a small opening in the hull. Although there is a zero net mass flux over a full pulsation cycle, the thrusters produce a positive flux of impulse and kinetic energy. Our group has extensively modelled the dynamics of the bioinspired thrusters in previous studies 38,48–50. Due to vehicle limitations, we suspended the vehicle from a floating raft. This was done to ensure that the vehicle could be fully submerged below the surface without the need for a high-speed active depth control system. However, the AUV in this configuration is only slightly negatively buoyant so the forces from the raft are minimal.

Modular lateral line system design. The new proposed control methodology requires that hydrodynamic forces acting on an AUV are directly measured in real time, so that the vehicle can compensate before being displaced. To measure the hydrodynamic forces acting on the prototype AUV, we constructed an artificial lateral line system that uses distributed sensors to measure the pressure distribution over the surface of the vehicle. Here, we will discuss the design of this sensory system and the algorithm for integrating the pressure distribution to calculate the hydrodynamic forces and moments acting on a rigid body.

We designed the artificial lateral line system to be modular, consisting of a 3D printed scaffolding that fastens custom sensor modules in place. The modular structure of this system confers several benefits. First, we did not need to make costly modifications to the existing AUV hull; rather, the lateral line system fits around the vehicle like a shell, as shown in Fig. 2. Second, the modular structure of the lateral line allows the system to be easily repaired and maintained. When a sensor module fails or the scaffolding breaks, it is easy to replace the damaged component. Finally, the modular design allows for flexibility; depending on the test, the lateral line could be reconfigured to enhance the sensitivity to different phenomena.

The basic sensing unit of our artificial lateral line system is a sensor module, as shown in Fig. 3. Each sensor module is composed of a custom printed circuit board with electronics embedded in Ecoflex 00-30 elastomer. The module contains two Freescale Semiconductor MPXV7002 differential pressure sensors. These sensors consist of a piezoresistive transducer, which measures pressure differences between two ports in the range of  $\pm 2$  kPa and has a sensitivity of 1.0 V kPa<sup>-1</sup>. The output of each sensor is connected to a tunable first-order analog filter composed of a capacitor and a digital potentiometer. The cutoff frequency of the filter can be tuned from 15.9 Hz to 1.59 kHz. The sensors have two main sources of noise; one source is electrical due to the effect of the motor's load on the vehicle power system, while the other is due to structural vibrations, which result in biased noise due to sensor internal asymmetry. However, both sources of noise occur at frequencies faster than the dynamic oscillation of surface pressure. The cutoff frequency is chosen based on the sampling frequency such that high-frequency components that would be aliased are attenuated. The filtered voltage is then sampled by a 12 bit analog-to-digital converter (ADC). Given the sensor sensitivity and resolution of the ADC, the overall resolution of the sensor module is  $\sim$ 1.22 Pa.

The electronics are then placed in a mould as shown in Fig. 3, submerged in elastomer and allowed to cure. This seals the boards, protecting them from being physically damaged as well as waterproofing the electronics and reduces noise due to vibration. Vinyl tubing connects the ports of the differential pressure sensors to the surface of the sensor module. The moulds are manufactured such that the length of the tubing is consistent and the tube opening is flush with the surface of the module. Each individual sensor is calibrated in the final assembled

configuration by holding the AUV at different configurations in a resting fluid environment and using vehicle orientation to calculate the hydrostatic pressure differential across each set of pressure ports. The method for calculating the hydrostatic pressure differential is presented in the following discussion. Additional details and results from sensor calibration are provided in the Supplementary Information. The sensors were observed to have a linear relationship between pressure differential and output voltage.

The entire lateral line system, including 18 sensor modules and the data-processing module, draws an average current of 0.323 A at the vehicle's 12 V main power, for an average power load of 3.876 W.

**Sensor distribution.** The sensor distribution of the artificial lateral line presented in this Article spans the section of the vehicle between the two sets of bioinspired thrusters (Fig. 2). The sensors are organized into two rings, each with six evenly spaced modules, covering the vehicle in the circumferential direction, with two lines of sensors, three sensor modules long, on both sides in between the rings.

The layout of the lateral line makes it sensitive to measuring sway and heave forces (body y and z, respectively), with very little to no sensitivity to surge forces (body x). In future iterations of this system, sensor arrays will be placed on the nose cone to provide this sensitivity. However, the goal of the current study is to experimentally validate the proposed control methodology. We therefore focused our analysis and limited disturbance forces to the sway direction, although the vehicle is free to move in all six DOFs.

**Force calculation.** The total hydrodynamic forces acting on the vehicle can be calculated from the pressure distribution on the surface of the vehicle, that is

$$\mathbf{F}_{\mathrm{D}} = \int_{S} P_{\mathrm{T}} \hat{\mathbf{n}} \, \mathrm{d}S \tag{6}$$

where  $\mathbf{F}_{\mathrm{D}}$  is the hydrodynamic force,  $P_{\mathrm{T}}$  is the total pressure distribution over the surface of the vehicle, and  $\hat{\mathbf{h}}$  is the unit vector normal to the surface. It should be noted that the hydrodynamic forces consist of both pressure and shear stresses; however, at the velocities encountered in this study the shear forces are negligible in comparison to the pressure forces and are therefore ignored.

The goal of the lateral line sensory system is to provide an estimate of the pressure distribution on the surface of the vehicle, with total pressure being the sum of the static pressure and dynamic pressure:

$$P_{\mathrm{T}}(\mathbf{x},t) = P_{\mathrm{S}}(\mathbf{x}) + P_{\mathrm{D}}(\mathbf{x},t) \tag{7}$$

In this equation,  $\mathbf{x}$  refers to the position on the vehicle surface, and t refers to time. The static component, due to the hydrostatic balance, is only a function of depth in the water column. The component of  $F_{\rm D}$  corresponding to the integration of  $P_{\rm S}$  is the buoyant force. Because this force is already being compensated by the weight force, for a neutrally buoyant vehicle, it should be left out of the control law.

Generally, gauge or absolute pressure sensors require a much larger sensing range than differential pressure sensors due to the large static pressures encountered at any appreciable depth. This dictates that these sensors have a lower sensitivity, as there is a trade-off between sensor range and sensitivity. Furthermore, the dynamic pressure is much smaller than the static pressure, requiring a high-sensitivity measurement. This means that static pressure sensors with the range necessary for use at any non-negligible depth will not have the required sensitivity to recover the dynamic pressure component. We have presented a more thorough analysis of the dynamic and static pressure trade-offs in ref. <sup>31</sup>.

One solution to this issue is to use differential pressure sensors, which, by nature of their design, reduce the effect of the static pressure on the measurement. Instead of measuring the absolute pressure at a point, differential pressure sensors (as their name suggests) measure the pressure difference between two ports. Thus, any static pressure measured by such a sensor is a function of the vertical separation of the ports. Thus, if the separation is small, the effect of the static component can be minimized. An algorithm for compensating for the remaining static component is presented in the next subsection.

**Static pressure component.** We use the AUV orientation during testing, measured by the motion capture system in real time, to calculate the hydrostatic pressure gradient across all of the pressure sensors. The line extending from one port to the other on any of the sensors can be defined in a body-fixed coordinate frame as  $|\delta|[0, -\cos(\gamma), -\sin(\gamma)]^T$ , where  $\gamma$  is the azimuthal position of the centre of the sensor and  $|\delta|$  is the linear distance between the two ports. After rotating this vector into the Earth-fixed reference frame, we isolate the vertical separation between the pressure ports:

$$\Delta h = -|\delta| \cos(\theta) [\sin(\phi)\cos(\gamma) + \cos(\phi)\sin(\gamma)]$$

$$|\delta| = R\sqrt{2(1-\cos(\alpha))}$$
(8)

where R is the AUV radius,  $\alpha$  is the angular separation of the two pressure ports (for the system in our testing this separation is 30°),  $\theta$  is the AUV roll angle and  $\phi$ 

NATURE MACHINE INTELLIGENCE ARTICLES

is the AUV pitch angle. The pressure gradient due to hydrostatic pressure is then  $\rho g \Delta h$ , where  $\rho$  is the fluid density and g is gravitational acceleration. The static pressure gradient is subtracted from the sensor measurement before calculating the hydrodynamic forces.

**Fourier fitting and dynamic pressure.** We recognize that, due to the physical constraints and vehicle geometry, the pressure distribution over the vehicle needs to be a periodic function of the azimuthal angle  $\gamma$ , and therefore should be well approximated by a Fourier series representation. The generic pressure distribution at some axial location is given in terms of the Fourier coefficients  $a_n$  and  $b_n$ :

$$P_{\gamma} = \sum_{n=1}^{N} a_n \sin(n\gamma) + b_n \cos(n\gamma)$$
 (9)

where N is the maximum wavenumber considered. From this series we can calculate the pressure difference across two ports of a pressure sensor at angle  $\gamma$  with port separation  $\alpha$ :

$$\Delta P = P\left(\gamma + \frac{\alpha}{2}\right) - P\left(\gamma - \frac{\alpha}{2}\right)$$

$$= \sum_{n=1}^{N} a_n \left[ \sin\left(n\left(\gamma + \frac{\alpha}{2}\right)\right) - \sin\left(n\left(\gamma - \frac{\alpha}{2}\right)\right) \right]$$

$$+ b_n \left[ \cos\left(n\left(\gamma + \frac{\alpha}{2}\right)\right) - \cos\left(n\left(\gamma - \frac{\alpha}{2}\right)\right) \right]$$
(10)

If there are m pressure sensors at a given axial location and at angles  $\gamma_m$ , then we can write a set of m linear equations for the pressure differences:

$$\begin{bmatrix} \Delta P_1 \\ \Delta P_2 \\ \vdots \\ \Delta P_m \end{bmatrix} = \begin{bmatrix} A_{F1} & A_{F2} \\ A_{F3} & A_{F4} \end{bmatrix} \cdot \begin{bmatrix} a_1 \\ a_2 \\ \vdots \\ b_1 \\ b_2 \\ \vdots \end{bmatrix}$$

$$(11)$$

$$\begin{split} A_{\mathrm{F}1} &= \begin{bmatrix} 2\cos(\gamma_1)\sin\left(\frac{\alpha}{2}\right) & 2\cos(2\gamma_1)\sin(\alpha) & \dots \\ 2\cos(\gamma_2)\sin\left(\frac{\alpha}{2}\right) & 2\cos(2\gamma_2)\sin(\alpha) & \dots \\ & \vdots & & \ddots \end{bmatrix} \\ A_{\mathrm{F}2} &= \begin{bmatrix} -2\sin(\gamma_1)\sin\left(\frac{\alpha}{2}\right) & -2\sin(2\gamma_1)\sin(\alpha) & \dots \\ -2\sin(\gamma_2)\sin\left(\frac{\alpha}{2}\right) & -2\sin(2\gamma_2)\sin(\alpha) & \dots \\ & \vdots & & \ddots \end{bmatrix} \\ A_{\mathrm{F}3} &= \begin{bmatrix} 2\cos(\gamma_m)\sin\left(\frac{\alpha}{2}\right) & 2\cos(2\gamma_m)\sin(\alpha) & \dots \end{bmatrix} \\ A_{\mathrm{F}4} &= \begin{bmatrix} -2\sin(\gamma_m)\sin\left(\frac{\alpha}{2}\right) & -2\sin(2\gamma_m)\sin(\alpha) & \dots \end{bmatrix} \end{split}$$

Here,  $A_{E}$  is an  $m \times 2N$  array. Therefore, the vector of Fourier coefficients can be solved as  $(A_{\rm F})^{-1}\Delta P$ . Both the number of wavemodes included in the Fourier series, N, and the number of sensors at a given axial location, m, are constraints that must be selected by the system designer, but note that, by the Nyquist criterion, the number of wavemodes included cannot exceed half the number of sensors. Furthermore, if N is less than m/2,  $(A_F)^{-1}$  must be calculated by one of many pseudo-inverse algorithms to provide a least-squares fit. For the system utilized in this study, sensors are arranged into rings around the AUV, with each ring consisting of six sensors. We fit the pressure gradient distribution to a Fourier series with a maximum wavenumber of 3, so that at each instant in time the Fourier coefficients are an exact solution for the measured pressure gradient values. It should be noted here that the Fourier fitting of the pressure distribution can be used as an additional mechanism for filtering both electrical noise in the signals and the turbulent noise in the pressure distribution itself. If a designer is anticipating a particularly noisy environment, the sensing system should be allocated with more sensor modules than twice the desired number of resolved wavemodes. In addition, the number of resolved wavemodes can be reduced to allow Fourier coefficient fitting in the event of sensor failure, as described in the section 'Impact of sensor failure,' in the Supplementary Information.

The force in the sway direction on any differential surface element is the product of the local pressure and the projection of the normal vector onto the sway axis. Integrating this around the vehicle in the azimuthal direction gives the force

density in the sway direction, which is the sway force per unit length at this axial location. The force density only depends on the first Fourier coefficient,  $a_1$ , due to the symmetry of the other modes:

$$\frac{\mathrm{d}F_{y}}{\mathrm{d}x} = \oint_{0}^{2\pi} P_{y}\hat{\mathbf{y}} \cdot \hat{\mathbf{n}}r \,\mathrm{d}\gamma = -\pi R a_{1} \tag{12}$$

In this equation,  $F_y$  is the component of  $\mathbf{F}_D$  in the y axis and  $\hat{\mathbf{y}}$  is the unit vector in the sway direction.

As a first-order estimate, the geometry of the vehicle is approximated as a cylinder. At each cross-section of that cylinder, the force density can be calculated from corresponding Fourier coefficients at that location according to equation (12). Therefore the total force in the sway direction is just the integral of the force density and the total yaw torque is the integral of the force density multiplied by moment arm:

$$F_{y} = \int_{-L/2}^{L/2} \frac{dF_{y}}{dx} dx = -\pi R \int_{-L/2}^{L/2} a_{1}(x) dx$$

$$\tau_{r} = \int_{-L/2}^{L/2} \frac{dF_{y}}{dx} x dx = -\pi R \int_{-L/2}^{L/2} a_{1}(x) x dx$$
(13)

The prototype lateral line shell measures pressures and fits to a Fourier series at two axial locations, which we will denote with coefficients  $a_{1+}$  and  $a_{1-}$ . Assuming a linear force density along the axial direction allows the total sway force and yaw torque to be estimated from the two Fourier coefficients:

$$\begin{split} F_{y} &\approx -\pi R L \frac{a_{1+} + a_{1-}}{2} \\ \tau_{r} &\approx -\pi R \frac{L^{3}}{12} \frac{a_{1+} - a_{1-}}{d_{ring}} \end{split} \tag{14}$$

where  $d_{\rm ring}$  is the axial distance between the two sensor rings (0.42 m for the prototype system). In general, the pressure distribution will not be uniform along the surface of the vehicle. By considering both sets of rings, we achieve a more accurate estimation of the force.

Lateral line vehicle integration. CephaloBot was designed to be both a technology demonstrator for the novel propulsion mechanism as well as a fully integrated autonomous platform for sensor and control experiments. A National Instruments (NI) Single-Board RIO (sbRIO) served as the main processor for the vehicle. The sbRIO communicates with the central microprocessor of the lateral line system using universal asynchronous receiver/transmitter (UART) communication at a frequency of  $\sim\!\!30\,\text{Hz}$ . The sbRIO runs the control loop at an average frequency of  $\sim\!\!10\,\text{Hz}$ , communicating wirelessly with the desktop computer located on the platform above the testing tank. Because the microprocessor-to-sbRIO communication is faster than the vehicle-to-desktop communication, the sbRIO keeps a running average for each sensor before sending the averaged values to the motion controller.

The motion controller uses localization information from the motion capture system to calculate the position and velocity state error. The feedback and feedforward terms are added together to produce the total desired control force on the vehicle. This control force is mapped to the desired control signals for each thruster and sent to individual motor controller boards.

The lateral line system is connected to CephaloBot with a waterproof Ethernet cable, receiving power from the vehicle and communicating with the on-board sbRIO using UART over an RS-485 architecture. The lateral line sensor modules are connected to the centralized processor module of the lateral line system and communicate with it via a parallel implementation<sup>31</sup> of the Inter-Integrated Circuit (I<sup>2</sup>C) communication protocol. The parallel communication architecture ensures that the ADCs begin voltage conversion simultaneously, removing the need for temporal correction.

### Data availability

Any data gathered and reported in this study can be provided by the corresponding author upon request.

Received: 6 August 2018; Accepted: 15 March 2019; Published online: 22 April 2019

# References

- Bellingham, J. G. & Wilcox, J. S. Optimizing AUV oceanagraphic surveys. In Proc. IEEE/OES Symposium on Autonomous Underwater Vehicle Technology 391–398 (IEEE, 1996).
- 2. Whitcomb, L. L., Yoerger, D. R., Singh, H. & Mindell, D. A. Towards precision robotic maneuvering, survey, and manipulation in unstructured

- undersea environments. In *Proc. International Symposium on Robotics Research* 45–54 (Springer, 1998).
- Yoerger, D. & Slotine, J. J. E. Adaptive sliding control of and experimental underwater vehicle. In *Proc. IEEE International Conference on Robotics and Automation (ICRA)* 2746–2751 (IEEE, 1991).
- Martin, S. C. & Whitcomb, L. L. Fully actuated model-based control with six-degree-of-freedom coupled dynamical plant models for underwater vehicles: theory and experimental evaluation. *Int. J. Robot. Res.* 35, 1164–1184 (2016).
- Liao, J. C. A review of fish swimming mechanics and behaviour in altered flows. *Philos. Trans. R. Soc. B* 362, 1973–1993 (2007).
- Blaxter, J. H. S. Structure and development of the lateral line. Biol. Rev. 62, 471–514 (1987).
- Pitcher, T. J., Partridge, B. L. & Wardle, C. S. A blind fish can school. Science 194, 963–965 (1976).
- 8. Coombs, S. Smart skins: information processing by lateral line sensors. *Auton. Robots* 11, 225–261 (2001).
- Bleckmann, H. Peripheral and central processing of lateral line information. J. Comp. Physiol. A 194, 145–158 (2008).
- Montgomery, J. C. & Macdonald, J. A. Sensory tuning of lateral line receptors in Antarctic fish to the movement of planktonic prey. *Science* 235, 195–196 (1987).
- Pohlmann, K., Atema, J. & Breithaupt, T. The importance of the lateral line in nocturnal predation of piscivorous catfish. *J. Exp. Biol.* 207, 2971–2978 (2004).
- Satou, M. et al. Behavioral and electrophysiological evidences that the lateral line is involved in the inter-sexual vibrational communication of the himé salmon (landlocked red salmon, *Oncorhynchus nerka*). *J. Comp. Physiol. A* 174, 539–549 (1994).
- Kroese, A. B. A., Van der Zalm, J. M., Van & den Bercken, J. Frequency response of the lateral-line organ of *Xenopus laevis*. *Pflügers Arch.* 375, 167–175 (1978).
- Coombs, S. & Montgomery, J. Function and evolution of superficial neuromasts in an Antarctic notothenioid fish. *Brain Behav. Evol.* 44, 287–298 (1994).
- 15. Munz, H. in The Mechanosensory Lateral Line 285-297 (Springer, 1989).
- Fan, Z. et al. Design and fabrication of artificial lateral line flow sensors. J. Micromech. Microeng. 12, 655–661 (2002).
- Kottapalli, A. G. P. et al. A liquid crystal polymer membrane MEMS sensor for flow rate and flow direction sensing applications. *J. Micromech. Microeng.* 21, 085006 (2011).
- Dagamseh, A., Wiegerink, R., Lammerink, T. & Krijnen, G. Imaging dipole flow sources using an artificial lateral-line system made of biomimetic hair flow sensors. J. R. Soc. Interface 10, 20130162 (2013).
- Abdulsadda, A. T. & Tan, X. Underwater tracking of a moving dipole source using an artificial lateral line: algorithm and experimental validation with ionic polymer–metal composite flow sensors. Smart Mater. Struct. 22, 045010 (2013).
- Fernandez, V. I. et al. Lateral-line-inspired sensor arrays for navigation and object identification. Mar. Technol. Soc. J. 45, 130–146 (2011).
- Chambers, L. et al. A fish perspective: detecting flow features while moving using an artificial lateral line in steady and unsteady flow. J. R. Soc. Interface 11, 20140467 (2014).
- Ren, Z. & Mohseni, K. A model of the lateral line of fish for vortex sensing. Bioinspir. Biomim. 7, 036016 (2012).
- Ren, Z. & Mohseni, K. Wall detection by lateral line sensory system of fish. In Proc. AIAA Aerospace Sciences Meeting 2014-0072 (AIAA, 2014).
- Xu, Y. & Mohseni, K. A pressure sensory system inspired by the fish lateral line: hydrodynamic force estimation and wall detection. *IEEE J. Ocean. Eng.* 42, 532–543 (2016).
- Xu, Y. & Mohseni, K. Bio-inspired hydrodynamic force feed forward for autonomous underwater vehicle control. *IEEE ASME Trans. Mechatron.* 19, 1127–1137 (2014).
- Akanyeti, O. et al. Self-motion effects on hydrodynamic pressure sensing: part I. Forward-backward motion. Bioinspir. Biomim. 8, 026001 (2013).
- Kottapalli, A. G. P., Asadnia, M., Miao, J. M., Barbastathis, G. & Triantafyllou, M. S. A flexible liquid crystal polymer MEMS pressure sensor array for fish-like underwater sensing. Smart Mater. Struct. 21, 115030 (2012).
- Paley, D. A. & Free, B. A. Model-based observer and feedback control design for a rigid Joukowski foil in a Karman vortex street. *Bioinspir. Biomim.* 13, 035001 (2018).
- 29. Arnold, G. P. Rheotrophism in fishes. Biol. Rev. 49, 515–576 (1974).
- Montgomery, J. C., Baker, C. F. & Carton, A. G. The lateral line can mediate rheotaxis in fish. *Nature* 389, 960–963 (1997).
- Nelson, K. & Mohseni, K. Design of a 3-D printed, modular lateral line sensory system for hydrodynamic force estimation. *Mar. Technol. Soc. J.* 51, 103–115 (2017).

- Song, Z., Lipinski, D. & Mohseni, K. Multi-vehicle cooperation and nearly fuel-optimal flock guidance in strong background flows. *Ocean Eng.* 141, 388–404 (2017).
- Song, Z. & Mohseni, K. Long-term inertial navigation aided by dynamics of flow field features. *IEEE J. Ocean. Eng.* 43, 940–954 (2017).
- 34. Fossen, T. I. Guidance and Control of Ocean Vehicles (Wiley, 1994).
- Paull, L., Saeedi, S., Seto, M. & Li, H. Auv navigation and localization: a review. IEEE J. Ocean. Eng. 39, 131–149 (2014).
- 36. Ruiz, I. T., de Raucourt, S., Petillot, Y. & Lane, D. Concurrent mapping and localization using sidescan sonar. *IEEE J. Ocean. Eng.* 29, 442–456 (2004).
- Eustice, R. M., Singh, H., Leonard, J. J. & Walter, M. R. Visually mapping the RMS titanic: conservative covariance estimates for SLAM information filters. *Int. J. Robot. Res.* 25, 1223–1242 (2006).
- Krieg, M. & Mohseni, K. Dynamic modeling and control of biologically inspired vortex ring thrusters for underwater robot locomotion. *IEEE Trans. Robot.* 26, 542–554 (2010).
- Antonelli, G., Caccavale, F., Chiaverini, S. & Villani, L. Tracking control for underwater vehicle-manipulator systems with velocity estimation. *IEEE J. Ocean. Eng.* 25, 399–413 (2000).
- Yoerger, D. & Slotine, J. Robust trajectory control of underwater vehicles. IEEE J. Ocean. Eng. 10, 462–470 (1985).
- Healey, A. J. & Lienard, D. Multivariable sliding mode control for autonomous diving and steering of unmanned underwater vehicles. *IEEE J. Ocean. Eng.* 18, 327–339 (1993).
- Yuh, J. Modeling and control of underwater robotic vehicles. IEEE Trans. Syst. Man Cybern. 20, 1475–1483 (1990).
- Marco, D. B. & Healey, A. J. Local area navigation using sonar feature extraction and model-based predictive control. *Int. J. Syst. Sci.* 29, 1123–1133 (1998).
- Kim, T. W. & Yuh, J. A novel neuro-fuzzy controller for autonomous underwater vehicles. In *Proc. International Conference on Robotics and Automation* 2350–2355 (IEEE, 2001).
- Walters, P., Kamalapurkar, R., Voight, F., Schwartz, E. M. & Dixon, W. E. Online approximate optimal station keeping of a marine craft in the presence of an irrotational current. *IEEE Trans. Robot.* 34, 486–496 (2018).
- Krieg, M., Klein, P., Hodgkinson, R. & Mohseni, K. A hybrid class underwater vehicle: bioinspired propulsion, embedded system, and acoustic communication and localization system. *Mar. Technol. Soc. J. Spec. Ed. Biomim. Mar. Technol.* 45, 153–164 (2011).
- Krieg, M., Nelson, K., Eisele, J. & Mohseni, K. Bioinspired jet propulsion for disturbance rejection of marine robots. *IEEE Robot. Autom. Lett.* 3, 2378–2385 (2018).
- Krieg, M. & Mohseni, K. Thrust characterization of pulsatile vortex ring generators for locomotion of underwater robots. *IEEE J. Ocean. Eng.* 33, 123–132 (2008).
- Krieg, M. & Mohseni, K. Modelling circulation, impulse and kinetic energy of starting jets with non-zero radial velocity. *J. Fluid Mech.* 719, 488–526 (2013).
- Krieg, M. & Mohseni, K. Pressure and work analysis of unsteady, deformable, axisymmetric, jet producing cavity bodies. *J. Fluid Mech.* 769, 337–368 (2015).

## Acknowledgements

This work was supported by the Office of Naval Research (ONR) and the National Science Foundation (NSF).

## **Author contributions**

M.K. helped design the prototype AUV and derived the force-processing algorithms. K.N. was responsible for all stages of system testing and helped design and validate the custom modular distributed pressure sensory system. K.M. supervised and provided advice for the entire research project, and helped edit and write the paper.

#### Competing interests

The authors declare no competing interests.

#### Additional information

 $\label{eq:Supplementary information} \textbf{Supplementary information} \ is available for this paper at \ https://doi.org/10.1038/s42256-019-0044-1.$ 

Reprints and permissions information is available at www.nature.com/reprints.

Correspondence and requests for materials should be addressed to K.M.

**Publisher's note:** Springer Nature remains neutral with regard to jurisdictional claims in published maps and institutional affiliations.

© The Author(s), under exclusive licence to Springer Nature Limited 2019